JOURNAL OF COMPUTATIONAL PHYSICS 17, 276–310 (1975)

Numerical Solution of the Navier–Stokes Equations with Topography

TZVI GAL-CHEN*

Advanced Study Program, National Center for Atmospheric Research,† Boulder, Colorado 80303

AND

RICHARD C. J. SOMERVILLE‡

Institute for Space Studies, Goddard Space Flight Center, NASA, New York, New York 10025

Received July 17, 1974; revised October 29, 1974

A finite difference scheme for solving the equations of fluid motion in a generalized coordinate system has been constructed. The scheme conserves mass and all the first integral moments of the motion. The scheme also advectively "almost conserves" second moments, in that the magnitude of implicit numerical smoothing is typically about an order smaller than explicit viscosity and diffusion. Calculations with the model support the theoretical conjecture that the difference scheme is stable whenever the analogous Cartesian scheme is stable. The scheme has been used to calculate dry atmospheric convection due to differential heating between top and bottom of mountainous terrain. The general small-scale characteristics of mountain up-slope winds have been simulated. In addition, the results have demonstrated the crucial role played by the eddy diffusivities and the environmental stability, in determining both the quantitative and the qualitative features of the circulation.

I. INTRODUCTION AND GENERAL APPROACH

In a previous paper [8], henceforth referred to as paper I, the authors have shown how a coordinate transformation may be utilized to solve numerically the Navier–Stokes equations with irregular lower boundary. The governing equations are then algebraically more complicated than their Cartesian analogs. Nevertheless, the boundary and the boundary conditions are simpler. This latter property makes it possible to employ many of the ideas and techniques of conventional difference

* Present address: Cooperative Institute for Research in Environmental Sciences (CIRES), University of Colorado, Boulder, CO 80302.

† The National Center for Atmospheric Research is sponsored by the National Science Foundation.

‡ Present address: National Center for Atmospheric Research, Boulder, CO 80303.

Copyright © 1975 by Academic Press, Inc.
All rights of reproduction in any form reserved.

schemes. Another advantage of the transformed approach is its ability to avoid singularities which result from the presence of obtuse boundary corners. These singularities are mathematically genuine, but unrealistic in many cases of physical interest in which the topography is smooth.

The numerical method to be described is, in principle, applicable to three space dimensions as well as to two. Our actual computations, however, are two-dimensional. We have felt that since the idea of using a coordinate transformation for the calculation of nonhydrostatic flow above a mountain is new, it should first be compared with previous calculations, which were done by using Cartesian coordinates. One such numerical simulation directly relevant to meteorology is that of Orville [20], and his calculations are two-dimensional.

One obvious advantage of two-dimensional calculations is that, taking into account limitations such as computer time and storage, two-dimensional calculations would permit better resolution per dimension. In fact, it has been concluded by Fox [6], who has carried out calculations in flat topography for three-dimensional shape-preserving convective elements, that three-dimensional calculations, with present computers, are only marginally possible. Our attitude is that it is necessary to understand the successes and limitations of three-dimensional dynamic simulations in flat topography before proceeding to three-dimensional calculations with topography.

It must be borne in mind, however, that some two-dimensional flows are intrinsically different from three-dimensional flows [16, 24]. The discrepancy becomes more and more severe as the Reynolds number increases. Thus the results of two-dimensional calculations could by no means be used to explain three-dimensional phenomena. However, no numerical approximations relevant to only two dimensions are used. In particular, we have used the "primitive" equations with velocity and pressure as dependent variables, rather than higher-order derived equations in which the vorticity and stream function are dependent variables. The viability of our method for three-dimensional calculations is therefore asserted.

In this paper we treat explicitly only the case of "free slip." The "free slip" case is numerically more difficult to deal with than the "no slip" case. However, it has the advantage of simplifying the boundary layer (see Discussion in Section 2.4 of paper I and also Eqs. (2-49-a-b) of paper I).

II. General Features of the Finite Difference Scheme

2.1. *Layout of Variables and Indices in the Mesh*

An Eulerian finite difference mesh in $(\bar{x}, \bar{z})$ space is shown in Fig. 1. For clarity we denote every transformed quantity by an overbar ($^-$). Thus u and w are the

velocities in the x, z direction, respectively, and $\bar{u}$, $\bar{w}$ are the contravariant components of the velocity vector in the $\bar{x}$, $\bar{z}$ direction, respectively. A typical cell is shown in more detail in Fig. 2.

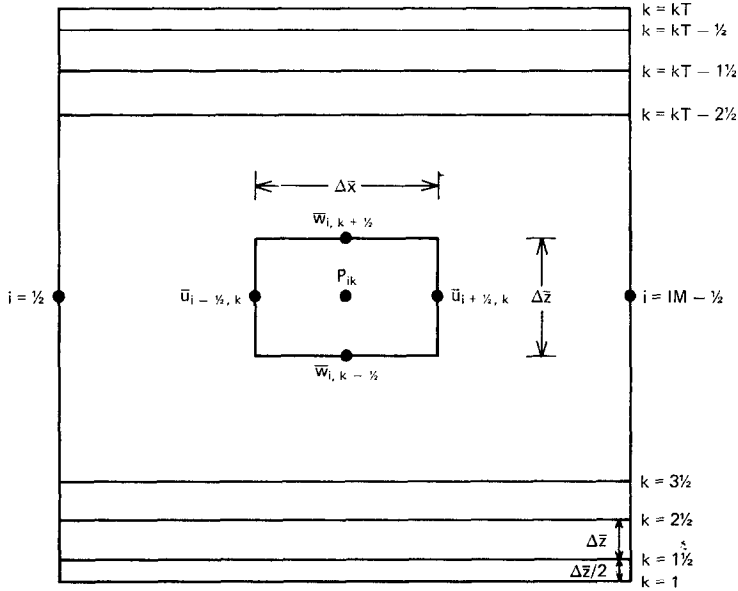

FIG. 1. An Eulerian mesh in the $(\bar{x}, \bar{z})$ space.

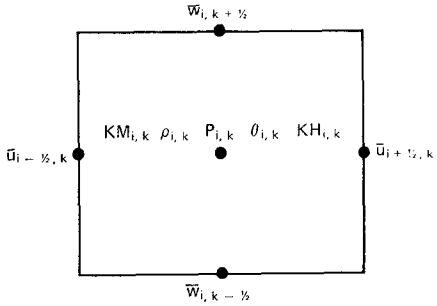

FIG. 2. Typical cell and locations of variables in the mesh.

The $\bar{x}$ coordinate is uniformly discretized at points $\bar{x}_i = (i - 1)\,\Delta x$, $i = 0, 1, \ldots, IM$. The $\bar{z}$ coordinate is discretized at points

$$\bar{z} = (k - 0.5)\,\Delta z, \qquad k = \tfrac{1}{2}, 1, 1.5, 2.5, \ldots, kT - \tfrac{1}{2}, kT, kT + \tfrac{1}{2},$$
$$\Delta\bar{z} = H/(kT - 1), \qquad \Delta\bar{x} = D/(IM - 1).$$

H and D are, respectively, the vertical and lateral extent of the computational domain.

The computational boundaries of the domain are from $i = \frac{1}{2}$ at the left to $i = IM - \frac{1}{2}$ at the right, and from $k = 1$ at the bottom to $k = kT$ at the top. Thus the grid is uniform in the $\bar{x}$ direction with width $\Delta\bar{x}$, but in the $\bar{z}$ direction the grid is uniform only at internal points. That is to say, the mesh width is $\Delta\bar{z}$ from $k = 1.5$ to $k = kT - \frac{1}{2}$, and at the bottom and top boundary, $k = 1$ and $k = kT$, the mesh width is $\Delta\bar{z}/2$. The physical domain is $(0, IM)$, and $(\frac{1}{2}, kT + \frac{1}{2})$.

We denote typical quantities at points $(\bar{x}_i, \bar{z}_j)$ as $\bar{f}_{ij}$. Thus

$$\bar{u}_{i+1/2,k} \equiv \bar{u}((i + \tfrac{1}{2} - 1)\,\Delta\bar{x}, (k - 0.5)\,\Delta\bar{z}), \text{ etc.}$$

In order to avoid confusion with contravariant indexing, which was used previously, all indices which are related to finite differencing are subscripted. $\bar{u}$ velocities are defined at grid points $(i + \frac{1}{2}, k)$, and $\bar{w}$ velocities at interior points are defined at cell edges $(i, k + \frac{1}{2})$. At the top and bottom boundary the condition $\bar{w}_{i,1} = \bar{w}_{i,kT} \equiv 0$ is imposed. Other quantities such as density ρ, pressure p, potential temperature θ, viscosity coefficient K_M (or KM), and diffusion coefficient K_H (or KH) are defined at cell centers (i, k).

The reason for halving the mesh width in the $\bar{z}$ direction, at the top and bottom boundary, is that we do not associate the points $(i, 1)$ at the boundary with the earth's surface, but rather postulate that a boundary layer of width $\Delta\bar{z}/2$ lies beneath the line $k = 1$. Frequently the temperature at boundary points $(i, 1)$ and a presumed ground temperature at points $(i, \frac{1}{2})$ are used to evaluate the normal heat flux at points $(i, 1)$. Note that the points $(i, \frac{1}{2})$ are beneath the computational domain. At the top boundary $(k = kT)$, and for a free-slip/rigid boundary condition, halving the mesh width merely means that $k = kT$ is an axis of symmetry, i.e., if

$$w_{i,kT} = 0,$$

then

$$w_{i,kT+1/2} = -w_{i,kT-1/2}\,,\ u_{i+1/2,kT-1} = u_{i+1/2,kT+1}\,.$$

Apart from the somewhat unusual treatment of the bottom and top boundary, this is the well-known staggered-mesh configuration introduced by Harlow and Welch [14]. Lilly [19] has shown that if one uses this configuration in a systematic way, quadratic quantities in finite-difference approximations to equations of conservation form are quasiconserved. It is important to emphasize that our transformed momentum equations (2-1) are not in strict conservation form, since extra nonderivative terms appear. Our temperature equation is in strict conservation form. It is also worth noting that in the schemes which quasiconserve quadratic quantities, numerical diffusion is eliminated [19]. This claim will remain true even if insufficient zoning is used. However, inadequate zoning will cause large truncation errors.

2.2. *Principle of the Finite Difference Scheme*

A. *Governing Equations*

Our momentum and continuity equations ((2-30), (2-31) of paper I) can be written as

$$(\partial/\partial\bar{x})(PX) + (\partial/\partial\bar{z})(PZ) = 0, \tag{2-1-a}$$

$$(\partial/\partial t)(PX) + FX(PX, PZ, \rho) = -PGX, \tag{2-1-b}$$

$$(\partial/\partial t)(PZ) + FZ(PX, PZ, \rho) = -PGZ + B(\theta), \tag{2-1-c}$$

where

$$PX \equiv \rho(G)^{1/2}\,\bar{u}, \qquad PZ \equiv \rho(G)^{1/2}\,\bar{w}, \tag{2-2-a}$$

$$PGX \equiv (\partial/\partial\bar{x})\,p + (\partial/\partial\bar{z})\,G^{13}p, \tag{2-2-b}$$

$$PGZ \equiv (\partial/\partial\bar{x})\,G^{13}p + (\partial/\partial\bar{z})\,G^{33}p + (CR)\,p, \tag{2-2-c}$$

$$(G)^{1/2}\,p \to p, \tag{2-2-d}$$

$$B(\theta) \equiv (\rho g/\theta_0)\,\theta, \tag{2-2-e}$$

$$CR \equiv \left\{ \begin{matrix} 3 \\ m\ n \end{matrix} \right\} G^{mn} = -\left[\frac{\partial^2 z_s}{\partial x^2}\,\frac{\bar{z} - H}{H - z_s} + \frac{2(\bar{z} - H)}{H - z_s}\left(\frac{\partial z_s}{\partial x}\right)^2\right], \tag{2-2-f}$$

$$FX(PX, PZ, \rho) \equiv \partial\bar{\tau}^{1j}/\partial\bar{x}^j, \tag{2-2-g}$$

$$FZ(PX, PZ, \rho) \equiv (\partial\bar{\tau}^{3j}/\partial\bar{x}^j) + \left\{ \begin{matrix} 3 \\ m\ n \end{matrix} \right\} \bar{\tau}^{mn}. \tag{2-2-h}$$

Here the tensorial notation with summation convention has been used. z_s is the topography; $G^{1/2}$, G^{ij}, $\{{}_m{}^3{}_n\}$ are the Jacobian of the transformation, the conjugate of the metric tensor and Christophel's symbols of the second kind, respectively. In general, they are prescribed functions of the topography and the specific transformation. $\bar{\tau}^{ij}$ is the combined momentum and stress tensors, in the transformed coordinates. $\rho = \rho(z) = \rho(\bar{x}, \bar{z})$ is the basic prescribed density. θ is the perturbation potential temperature, where the basic state is that of an hydrostatic adiabatic flow with constant potential temperature θ_0. p is the perturbation pressure and g is the gravitational acceleration. It is important to note that FX and FZ are independent of p. PGX and PGZ on the other hand, are functions of p alone.

The potential temperature equation may be written as

$$(\partial/\partial t)(\rho G^{1/2}\theta) + (\partial/\partial\bar{x}^i)(\rho G^{1/2}\bar{u}^i\theta) = \partial H^i/\partial\bar{x}^i, \tag{2-3-a}$$

$$\bar{H}^i = \rho G^{1/2} K_H G^{ij}(\partial\theta/\partial\bar{x}^j). \tag{2-3-b}$$

K_H is the eddy diffusion coefficient, which, in general, is nonlinear (e.g. Eqs. (2-9) and (2-14) of paper I, and Deardorff [3]).

The boundary conditions for the momentum equations are "free-slip/rigid". For our particular transformation (see paper I, Eqs. (2–49-a-b)), they may be written as:

$$\bar{u}^3 = \bar{w} = 0, \qquad \text{at} \quad \bar{z} = 0, \tag{2-4-a}$$

$$G^{k3}(\partial \bar{u}^m/\partial \bar{x}^k) = G^{im}(\partial \bar{u}^3/\partial \bar{x}^i) - (\partial G^{m3}/\partial \bar{x}^l)\,\bar{u}^l. \tag{2-4-b}$$

Similar equations may be written for the lateral boundaries. There the equations are Cartesian and $G^{ij} = \delta^{ij}$.

The potential temperature boundary conditions specify either the normal heat flux through the boundary, or the temperature on the boundaries, or a combination of both. Typically these boundary conditions are (see paper I, Eq. (2-50))

$$\theta)_{\bar{z}=0} = f(\bar{x}, \bar{y}, t), \tag{2-5-a}$$

or

$$\bar{H}^3)_{\bar{z}=0} = f(\bar{x}, \bar{y}, t). \tag{2-5-b}$$

In both cases $f(\bar{x}, \bar{y}, t)$ is a prescribed function. Similar equations may be written for the other boundaries.

The reader who is interested in a more detailed description of the governing equations and the boundary conditions should consult paper I and [7, (pp. 65–75 and 97–108].

B. *Finite Differencing*

We wish now to integrate the set defined by (2-1) so that from known quantities at time level n ($t_n = n\Delta t$), we can evaluate quantities at time level $n + 1$. The procedure will consist of two steps.

Step 1. Evaluation of intermediate quantities ( )*, at intermediate time-level $n + \alpha$, $0 \leqslant \alpha \leqslant 1$,

$$[((PX)^*_{i+1/2,k,n+\alpha} - (PX)_{i+1/2,k,n})/\Delta t] + \alpha(FX)^*_{i+1/2,k,n+\alpha} = -(1 - \alpha)(PGX)_{i+1/2,k,n}\,, \tag{2-6-a}$$

$$[((PZ)^*_{i,k+1/2,n+\alpha} - (PZ)_{i,k+1/2,n})/\Delta t] + \alpha(FZ)^*_{i,k+1/2,n+\alpha} = -(1 - \alpha)(PGZ)_{i,k+1/2,n} + \alpha B(0.5(\theta_{i,k+1,n} + \theta_{i,k,n})). \tag{2-6-b}$$

$(PX)^*$ and $(PZ)^*$ are seen to be approximations of order $1 + (1 - 2\alpha)$ to the momentum equations, but they do not satisfy the continuity equation; therefore we denote them ( )* to emphasize that they cannot be considered as a solution to the governing equations. Step 1 is implicit and can be solved by inverting tri-diagonal matrices, or by iterations. Note that in Step 1 the pressure terms are explicit.

Step $\bar{2}$.

$$[((PX)_{i+1/2,k,n+1} - (PX)_{i+1/2,k,n})/\Delta t] + (FX)^*_{i+1/2,k,n+\alpha}$$
$$= -[\alpha(PGX)_{i+1/2,k,n+1} + (1 - \alpha)(PGX)_{i+1/2,k,n}],$$

$$[((PZ)_{i,k+1/2,n+1} - (PZ)_{i,k+1/2,n})/\Delta t] + (FZ)^*_{i,k+1/2,n+\alpha}$$
$$= -[\alpha(PGZ)_{i,k+1/2,n+1} + (1 - \alpha)(PGZ)_{i,k+1/2,n}] + B(0.5(\theta_{i,k+1,n} + \theta_{i,k,n})).$$

In the case $\alpha = \frac{1}{2}$, Step $\bar{2}$ can be seen to be fully centered in space and time, with second-order accuracy in time and in space. If $\alpha > \frac{1}{2}$, the accuracy is $2 + (1 - 2\alpha)$. Step $\bar{2}$ is only of pedagogical value, since we subtract Step $\bar{2}$ from 1 and get the following.

Step 2.

$$[((PX)_{i+1/2,k,n+1} - (PX)^*_{i+1/2,k,n+\alpha})/\Delta t] + (1 - \alpha)(FX)^*_{i+1/2,k,n+\alpha}$$
$$= -\alpha(PGX)_{i+1/2,k,n+1}, \tag{2-7-a}$$

$$[((PZ)_{i,k+1/2,n+1} - (PZ)^*_{i,k+1/2,n+\alpha})/\Delta t] + (1 - \alpha)(FZ)^*_{i,k+1/2,n+\alpha}$$
$$= -\alpha(PGZ)_{i,k+1/2,n+1} + (1 - \alpha)B(0.5(\theta_{i,k+1,n} + \theta_{i,k,n})). \tag{2-7-b}$$

It is important to note that the buoyancy force $B(\theta)$ is evaluated at time level n. Therefore the temperature calculation can be separated from the momentum calculation.

C. *The Pressure Equation*

Step 2 involves the pressure gradients (PGX, PGZ) as unknown. In order to solve for the pressure, an additional equation is needed, namely some finite difference approximation to the continuity equation. A finite difference form of the continuity equation at every inner point is

$$[((PX)_{i+1/2,k,n+1} - (PX)_{i-1/2,k,n+1})/\Delta\bar{x}] + [((PZ)_{i,k+1/2,n+1} - (PZ)_{i,k-1/2,n+1})/\Delta\bar{z}]$$
$$\equiv 0. \tag{2-8}$$

In order to insure satisfaction of (2-8), we substitute (2-7) in (2-8) to get the pressure equation

$$F_{i,k,n+\alpha} = -\alpha\left[\frac{(PGX)_{i+1/2,k,n+1} - (PGX)_{i-1/2,k,n+1}}{\Delta\bar{x}} + \frac{(PGZ)_{i,k+1/2,n+1} - (PGZ)_{i,k-1/2,n+1}}{\Delta\bar{z}}\right], \tag{2-9}$$

where we have defined $F_{i,k,n+\alpha}$ as

$$F_{i,k,n+\alpha} = -\Big(\frac{(PX)^*_{i+1/2,k,n+\alpha} - (PX)^*_{i-1/2,k,n+\alpha}}{\Delta\bar{x}\,\Delta t} + \frac{(PZ)^*_{i,k+1/2,n+\alpha} - (PZ)^*_{i,k-1/2,n+\alpha}}{\Delta\bar{z}\,\Delta t}\Big) + (1-\alpha)\Big(\frac{(FX)^*_{i+1/2,k,n+\alpha} - (FX)^*_{i-1/2,k,n+\alpha}}{\Delta\bar{x}} + \frac{(FZ)^*_{i,k+1/2,n+\alpha} - (FZ)^*_{i,k-1/2,n+\alpha}}{\Delta\bar{z}}\Big) - (1-\alpha)\frac{B((\theta_{i,k+1,n} + \theta_{i,k,n})\,0.5) - B((\theta_{i,k,n} + \theta_{i,k-1,n})\,0.5)}{\Delta\bar{z}}. \quad (2\text{-}10)$$

To get the pressure equation in a more expanded form, let us now represent the pressure gradients at interior points explicitly.

$$(PGX)_{i+1/2,k} = \frac{p_{i+1,k} - p_{i,k}}{\Delta\bar{x}} + \frac{(G^{13}p)_{i+1,k+1} + (G^{13}p)_{i,k+1} - (G^{13}p)_{i+1,k-1} - (G^{13}p)_{i,k-1}}{4\,\Delta\bar{z}}, \quad (2\text{-}11\text{-a})$$

$$(PGZ)_{i,k+1/2} = \frac{(G^{33}p)_{i,k+1} - (G^{33}p)_{i,k}}{\Delta\bar{z}} + \frac{(G^{13}p)_{i+1,k+1} + (G^{13}p)_{i+1,k} - (G^{13}p)_{i-1,k+1} - (G^{13}p)_{i-1,k}}{4\,\Delta\bar{x}} + ((CR)_{i,k+1}\,p_{i,k+1} + (CR)_{i,k}\,p_{i,k})\cdot 0.5. \quad (2\text{-}11\text{-b})$$

Substituting (2-11) into (2-9) results in the pressure equation, for time level $n'+1$:

$$-\alpha\Big[\frac{p_{i+1,k,n+1} + 2p_{i,k,n+1} + p_{i-1,k,n+1}}{\Delta\bar{x}^2} + \frac{(G^{33}p)_{i,k+1,n+1} - 2(G^{33}p)_{i,k,n+1} + (G^{33}p)_{i,k-1,n+1}}{\Delta\bar{z}^2} + \frac{(G^{13}p)_{i+1,k+1,n+1} - (G^{13}p)_{i-1,k+1,n+1} - (G^{13}p)_{i+1,k-1,n+1} + (G^{13}p)_{i-1,k-1,n+1}}{2\,\Delta\bar{x}\,\Delta z} + 0.5\,\frac{(CR)_{i,k+1}\,p_{i,k+1,n+1} - (CR)_{i,k-1}\,p_{i,k-1,n+1}}{\Delta\bar{z}}\Big] = F_{i,k,n+\alpha}. \quad (2\text{-}12)$$

This pressure equation can be seen to be a finite difference analog of the pressure equation which one will get by applying the Div operator to the momentum equations.

At the boundaries, and at points neighboring the boundaries, modifications are sometimes needed, so that imposed boundary conditions are identically satisfied. In addition, one has to ensure mass continuity at the boundaries. Taking into account that at the boundaries, $k = 1$ and $k = kT$, the mesh width in the $\bar{z}$ direction is $\Delta\bar{z}/2$, we define the continuity equation at the bottom as

$$[((PX)_{i+1/2,1,n+1} - (PX)_{i-1/2,1,n+1})/\Delta\bar{x}] + [((PZ)_{i,1.5,n+1} - 0)/(\Delta\bar{z}/2)] \equiv 0. \quad (2\text{-}13)$$

Here we have imposed $(PZ)_{i,1} \equiv 0$. In order to insure satisfaction of (2-13), we have to substitute (2-7) in (2-13), as we did previously for interior points. To do so we need PGX at the boundary. Inspection of the definition of PGX in (2-2) reveals that, if the topography is not zero, both $\partial p/\partial\bar{x}$ and $\partial p/\partial\bar{z}$ are needed for evaluation of PGX. While $\partial p/\partial z$ can be obtained from the momentum equation for PZ, at $k = 1$, we have found it more practical to approximate PGX by

$$(PGX)_{i+1/2,1} = \frac{p_{i+1,1} - p_{i,1}}{\Delta\bar{x}} + \frac{(G^{13}p)_{i+1,2} + (G^{13}p)_{i,2} - (G^{13}p)_{i+1,1} - (G^{13}p)_{i,1}}{2\,\Delta\bar{z}}$$

$$- \frac{(G^{13}p)_{i+1,3} - 2(G^{13}p)_{i+1,2} + (G^{13}p)_{i+1,1}}{4\,\Delta\bar{z}}$$

$$- \frac{(G^{13}p)_{i,3} - 2(G^{13}p_{i,2} + (G^{13}p)_{i,1}}{4\,\Delta\bar{z}}. \quad (2\text{-}14)$$

PGX is therefore approximated to second-order accuracy. Now substituting (2-7) in (2-13), and using (2-14) for the definition of PGX, we get the pressure equation at $k = 1$:

$$F_{i,1,n+\alpha} = -\alpha\left[\frac{p_{i+1,1,n+1} - 2p_{i,1,n+1} + p_{i-1,1,n+1}}{\Delta\bar{x}^2} + \frac{2((G^{33}p)_{i,2,n+1} - (G^{33}p)_{i,1,n+1})}{\Delta\bar{z}^2}\right.$$

$$+ \frac{(CR)_{i,2}\,p_{i,2} + (CR)_{i,1}\,p_{i,1}}{\Delta\bar{z}} + \frac{1}{\Delta\bar{z}\,\Delta\bar{x}}((G^{13}p)_{i+1,2} - (G^{13}p)_{i-1,2})$$

$$- \frac{1}{4\,\Delta\bar{x}\,\Delta\bar{z}}((G^{13}p)_{i+1,3} - 2(G^{13}p)_{i+1,2} + (G^{13}p)_{i+1,1})$$

$$\left.\frac{1}{4\,\Delta\bar{x}\,\Delta\bar{z}}(G^{13}p)_{i-1,3} - 2(G^{13}p)_{i-1,2} + (G^{13}p)_{i-1,1}\right]. \quad (2\text{-}15)$$

$F_{i,1,n+\alpha}$ is defined as

$$F_{i,1,n+\alpha} = -\left(\frac{(PX)^*_{i+1/2,1,n+\alpha} - (PX)^*_{i-1/2,1,n+\alpha}}{\Delta\bar{x}\,\Delta t} + \frac{(PZ^*)_{i,1+1/2,n+1}}{\Delta\bar{z}/2\,\Delta t}\right)$$
$$+ (1-\alpha)\left(\frac{(FX^*)_{i+1/2,1,n+\alpha} - (FX^*)_{i-1/2,1,n+\alpha}}{\Delta\bar{x}} + \frac{(FZ^*)_{i,1+1/2}}{\Delta\bar{z}/2}\right)$$
$$- (1-\alpha)\frac{B((\theta_{i,2,n} + \theta_{i,1,n})\,0.5)}{\Delta\bar{z}/2}. \tag{2-16}$$

In the case of no topography we get

$$-\alpha\left[\frac{p_{i+1,1,n+1} - 2p_{i,1,n+1} + p_{i-1,1,n+1}}{\Delta\bar{x}^2} + \frac{(p_2 - p_1)}{\Delta\bar{z}^2}\right] = F_{i,1,n+\alpha}. \tag{2-17}$$

Equation (2-17) could of course be derived from (2-12) with the Neumann boundary condition $p_{i,2} = p_{i,0}$.

At the top boundary, the derivation of the pressure equation is somewhat different than at the bottom, because $G^{ij})_{k=kT} = 0$ when $i \neq j$ and $(CR)_{i,kT} = 0$ (see Eq. (2-2-f)). Thus,

$$(PGX)_{i+1/2,kT} = [(p_{i+1,kT} - p_{i,kT})/\Delta\bar{x}] + [(-(G^{13}p)_{i+1,kT-1} - (G^{13}p)_{i,kT-1})/2\Delta\bar{z}]. \tag{2-18}$$

Here a first-order approximation has been used to evaluate $(\partial/\partial\bar{z})(G^{13}p)_{k=kT}$. The pressure equation is, therefore,

$$-\alpha\left[\frac{p_{i+1,kT,n+1} - 2p_{i,kT,n+1} + p_{i-1,kT,n+1}}{\Delta\bar{x}^2} + \frac{2((G^{33}p)_{i,kT-1,n+1} - (G^{33}p)_{i,kT,n+1})}{\Delta\bar{z}^2}\right.$$
$$+ \frac{-(G^{13}p)_{i+1,kT-1,n+1} + (G^{13}p)_{i-1,kT-1,n+1}}{\Delta\bar{x}\,\Delta\bar{z}}$$
$$\left. + \frac{-0.5CR_{i,kT-1}p_{i,kT-1}}{0.5\Delta\bar{z}}\right] = F_{i,kT,n+\alpha}, \tag{2-19}$$

where $F_{i,kT,n+\alpha}$ has been defined as

$$F_{i,kT,n+\alpha} = \left(\frac{(PX)^*_{i+1/2,kT,n+\alpha} - (PX)^*_{i-1/2,kT,n+\alpha}}{\Delta\bar{x}\,\Delta t} + \frac{-(PZ)^*_{i,kT-1/2,n+\alpha}}{(\Delta\bar{z}/2)\Delta t}\right)$$
$$+ (1-\alpha)\left(\frac{(FX)^*_{i+1/2,kT,n+\alpha} - (FX)^*_{i-1/2,kT,n+\alpha}}{\Delta\bar{x}} + \frac{-(FZ)^*_{i,kT-1/2,n+\alpha}}{\Delta\bar{z}/2}\right)$$
$$- (1-\alpha)\frac{-B((\theta_{i,kT,n} + \theta_{i,kT-1,n})\cdot 0.5)}{\Delta\bar{z}/2}. \tag{2-20}$$

Alternatively we could approximate the Laplacian by using Eq. (2-12), and defining pressure at the exterior points $(i, kT + 1)$. We would then have Eq. (2-12) with $F_{i,kT,n+\alpha}$ defined by (2-20) and with the boundary conditions

$$p_{i,kT+1,n+1} = p_{i,kT-1,n+1}\,, \tag{2-21-a}$$

$$(G^{33})_{i,kT+1} = (G^{33})_{i,kT-1}\,, \qquad (G^{13})_{i,kT+1} = -(G^{13})_{i,kT-1}\,, \tag{2-21-b}$$

$$(CR)_{i,kT+1} = -(CR)_{i,kT-1}\,. \tag{2-21-c}$$

Substitution of (2-21) in (2-12) will give (2-19).

At the lateral boundaries $G^{ij} = \delta^{ij}$, and since the mesh width is uniform in the $\bar{x}$ direction, we use (2-12) without modification. The boundary conditions at the lateral boundaries are

$$p_{0,k} = p_{1,k}\,, \qquad p_{IM,k} = p_{IM-1,k}\,, \tag{2-22-a}$$

$$\bar{w}_{1,k+1/2} = \bar{w}_{0,k+1/2}\,, \qquad \bar{w}_{IM-1,k} = \bar{w}_{IM,k}\,, \tag{2-22-b}$$

$$\bar{u}_{1/2,k} = 0, \qquad \bar{u}_{IM-1/2,k} = 0, \tag{2-22-c}$$

$$\theta_{0,k} = \theta_{1,k}\,, \qquad \theta_{IM,k} = \theta_{IM-1,k}\,. \tag{2-22-d}$$

These boundary conditions give the pressure boundary condition, and allow for the calculation of $F_{i,k}$, as well as $(FX)_{i+1/2,k}$, $(FZ)_{i,k+1/2}$ at the lateral boundaries.

D. *Comparison with Some "Standard" Cartesian Schemes*

In the case of no-topography, our scheme is a combination of several "standard" Cartesian schemes.

If Step 1 were fully explicit, i.e.,

$$(FX^*)_{i+1/2,k,n+\alpha} = (FX)_{i+1/2,k,n}\,, \qquad (FZ^*)_{i,k+1/2,n+\alpha} = (FZ)_{i,k+1/2,n}\,,$$

our scheme would have been a special case of the ICE method of Harlow and Amsden [13]. If, in addition, the condition $\alpha = 1$ were to be imposed, this would correspond to the MAC method of Harlow and Welch [14]. In either case, if viscosity and diffusion were set to zero, and no iterations were used, the method would be linearly unstable.

If Step 1 were fully implicit, and $\alpha = 1$ (i.e., the solution would have been obtained by inverting matrices), this would correspond, apart from a slight modification at the boundaries, to a staggered variant of the Chorin [1] scheme. Actually the Chorin prescription could have been implemented just as well with $1 \geqslant \alpha \geqslant \frac{1}{2}$.

If the time derivative were evaluated using the leap-frog scheme, the advective terms evaluated explicitly at time level n, and the diffusive terms evaluated at time level $n - 1$, this would essentially correspond to a scheme used by Williams [27], Deardorff [2], Fox [6], and Steiner [25]. This scheme is second-order in time and

space, only with respect to the advective terms. It is second-order in space and first-order in time with respect to the diffusive terms. The advantages of the leap-frog scheme are that it is economical and does not contain implicit built-in smoothing. Thus in the absence of viscosity and diffusion, the staggered variant of the leap-frog will ensure quasi-conservation of quadratic quantities. The disadvantages of the leap-frog scheme are that it contains a spurious (splitting) solution in time [19], and thus an occasional forward time step is needed. In addition it has been shown by Kreiss and Oliger [17] that this scheme is nonlinearly unstable with respect to certain perturbations.

In the case $\alpha = \frac{1}{2}$ our scheme, being a variant of the Crank–Nicholson scheme, will not contain implicit smoothing. In addition it does not possess a spurious solution in time. For $\alpha > \frac{1}{2}$ implicit smoothing is introduced. If this implicit smoothing is much less than the explicit smoothing given by the nonlinear eddy viscosity concept [3, 7], this is useful because it can help control nonlinear instabilities.

A scheme which genuinely conserves quadratic quantities is always stable, by definition. In the case of a staggered mesh, this can be achieved with the Crank–Nicholson scheme [22, p. 189], in which typical spatial terms, $f_{i,j,n+1/2}$ at time level $n + \frac{1}{2}$ are represented as

$$f_{i,j,n+1/2} = 0.5\,(f_{i,j,n} + f_{i,j,n+1}).$$

Since $f^*_{i,j,n+1/2}$ from Step 1 (Eqs. (2-6-a-b)) is a better approximation to

$$0.5\,(f_{i,j,n} + f_{i,j,n+1}) \text{ than } f_{i,j,n}$$

alone, our scheme will presumably conserve quadratic quantities better than the leap-frog scheme.

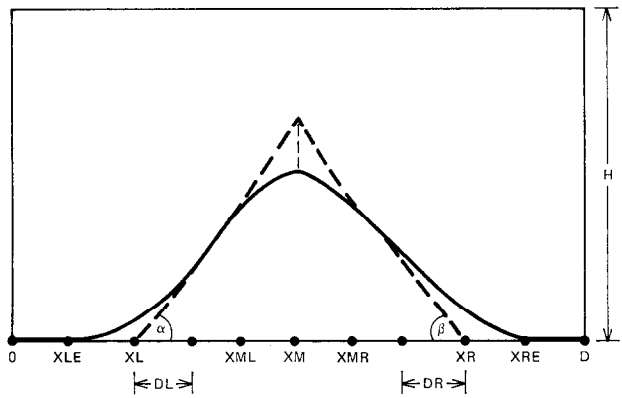

FIG. 3. Schematic representations of the topography (solid line), approximating the piecewise linear ridge (dashed line) with slopes α, β. For definitions of other symbols, see text.

2.3. *Evaluation of* $(FX)^*$, $(FZ)^*$, $B(\theta)$, *and the Temperature Equation*

Based on the staggered configuration shown in Figs. 1 and 2, the evaluation of the spatial terms is straightforward. The various terms are approximated by finite differences over one grid interval. If a quantity is needed at grid points where it is not defined, it is approximated by linear interpolation. The details, which are in fact a straightforward application of the MAC prescription, can be found in [7].

2.4. *Summary of the Calculational Procedures*

The full algorithm can be now summarized as follows.

(1) For given PX and PZ at previous time step, calculate $(PGX)_{i+1/2,k,n}$ and $(PGZ)_{i,k+1/2,n}$ using (2-11) for interior and lateral boundary points, (2-14) for lower boundary points, and (2-18) for the top boundary. Since the buoyancy force is not part of the iteration, calculate $B(\theta)$ before starting the iterations.

(2) Solve iteratively Eqs. (2-6-a-b). The iterations can be viewed as an iterative solution, for a system of nonlinear algebraic equations. The system can be written symbolically as

$$f = r(f),$$

and the simplest iteration technique is

$$f^{m+1} = r(f^{(m)}), \qquad m = 1,\ldots, p.$$

No more than three or four iterations are used in practice, since even in the absence of full convergence, Eqs. (2-6-a-b) are an approximation of order $2(1-\alpha)$ to the governing equation.

(3) Evaluate $F_{i,k,n+\alpha}$ by using (2-10) at interior points and lateral boundaries, (2-16) at the lower boundary, and (2-20) at the upper boundary.

(4) Solve the elliptic pressure equation defined by (2-12) and (2-15). If Eq. (2-12) is used for the top boundary, the boundary condition (2-21) should be imposed. If no explicit boundary condition is given at the top, (2-19) should be used. The Eq. (2-12) could be solved by direct methods [23], but in the present work the solution has been obtained by relaxation techniques [1, 5, 26]. The choice of an optimal relaxation factor is crucial to the rate of convergence. While in some cases one can determine analytically the relaxation factor, in most cases this is done empirically, as a function of the number of mesh points, the specific transformation and the grid size. At any rate the finite difference analog of the pressure equation is singular, but this does not affect the convergence [15].

(5) Compute $(PX)_{i+1/2,k,n+1}$, and $(PZ)_{i,k+1/2,n+1}$ from (2-7).

(6) Using the advanced-time, Jacobian-weighted contravariant components of the momentum vector PX and PZ, solve iteratively the finite difference analog of the temperature equation (2-3-a-b) by the two-step method outlined previously. No more than three to four iterations are used. Here we use a parameter β,

$$0.5 \leqslant \beta \leqslant 1, \tag{2-23}$$

to control implicit smoothing, analogously to α in Eqs. (2-6) and (2-7).

This completes one cycle. At this stage, the governing equations are satisfied to second-order accuracy in space at every interior point, and to first-order accuracy at the boundaries. The accuracy in time is $2 + (1 - 2\alpha)$ for the momentum equations, and $2 + (1 - 2\beta)$ for the temperature equation. The parameters

$$1 \geqslant (\alpha, \beta) \geqslant \tfrac{1}{2}, \tag{2-24}$$

are used to control implicit built-in smoothing. For $\alpha = \beta = \frac{1}{2}$ no implicit smoothing is present.

2.5. *Some Heuristic Remarks on Stability, Convergence, Truncation Errors and Numerical Diffusion*

The stability and convergence of our scheme are not fully explored even for the case of no-topography. The numerical evidence, however, shows that the scheme is stable whenever its analogous Cartesian scheme is stable. There are several reasons why we have been hardly surprised by this result. First we note that the physics is unaltered by our transformation, and second that the transformation is nonsingular. Thus, if we had a uniform mesh in the $\bar{x}$, $\bar{z}$ directions defined by $\bar{\Delta}$, then we have a nonuniform mesh in the x, z direction. Let us now find a lower bound min Δ for the size of the mesh as measured in the (x, z) plane. In general

$$G^{1/2}\, d\bar{x}\, d\bar{y}\, d\bar{z} \approx dx\, dy\, dz.$$

Thus,

$$\min \Delta \approx \min(G^{1/2})^{1/3}\, \bar{\Delta}.$$

For our particular transformation

$$G^{1/2} = (H - z_s)/H < 1.$$

Thus $\min \Delta \approx (\min G^{1/2})\, \bar{\Delta}$ is a safe estimate. The classical Courant–Friedrichs–Lewy (CFL) condition for linear stability with respect to the advective terms reads in a Cartesian mesh for velocity $\mathbf{u}$ as

$$b \mid \mathbf{u} \mid \Delta t/(d^{1/2} \min \Delta) \leqslant 1,$$

or

$$b \mid \mathbf{u} \mid \Delta t/(d^{1/2} G^{1/2} \bar{\Delta}) \leqslant 1. \tag{2-25}$$

b is a constant of order unity which depends on the particular difference scheme, and d is the space dimension. It must be emphasized again that

$$| \mathbf{u} | \neq (\bar{u}^2 + \bar{w}^2)^{1/2}, \qquad \text{but} \quad | \mathbf{u} | = (u^2 + w^2)^{1/2}.$$

For the diffusive and dissipative terms, similar heuristic arguments will lead to the stability condition

$$bK \Delta t/((G^{1/2})^2 \bar{\Delta}^2) \leqslant 1/2d. \tag{2-26}$$

K is the viscosity or diffusion coefficient.

Having indicated that the linear stability properties of our scheme are essentially those of its analogous Cartesian scheme, the next logical question is what are the linear stability properties of the scheme in the absence of topography. Consideration must also be given to the linear stability of the combined two steps. For the case $\alpha = \beta = \frac{1}{2}$ the combined two steps can be seen to be an iterative solution of the Crank–Nicholson scheme. According to Gary [9], in order to ensure the stability of the scheme with respect to the advective terms, $b = \frac{1}{2}\alpha$, and the number of iterations has to be chosen from the sequence 3, 4, 7, 8, 11, 12. Similar analysis with respect to the diffusive terms shows that condition (2-26) with $b = 1$ is sufficient for stability for any number of iterations. In fact, $\frac{1}{2} \leqslant b \leqslant 1$ is permitted for the combined two steps as far as stability is concerned, but in this case the iterations of Step 1 will not converge. Thus, we will not be able to claim that we have solved iteratively Eqs. (2-3). If one is not too much concerned about second-order accuracy in time, one can treat the diffusive terms explicitly and iterate only on the convective terms. Gustafsson [12] has used a form of Gary's scheme for two-dimensional calculations of the shallow-water equations and has obtained satisfactory results.

In order for the method of transformed coordinates to be a viable alternative to the more straightforward approach of using Cartesian coordinates, it must satisfy the following practical requirements.

(a) Truncation errors, with and without topography, should be of the same order of magnitude.

(b) The time step, with and without topography, should be of the same order of magnitude.

(c) While a decrease in the calculational speed is expected due to the need to calculate extra terms, it is highly desirable that for a given accuracy the amount of pressure iterations, with and without topography, will be roughly the same.

In paper I it has been shown that, in order for requirements (a)–(c) to be met, one must specify a nonsingular transformation with a topography continuous up to

second derivatives. Equations (2-25) and (2-26) reveal that an additional constraint for our particular transformation is

$$G^{1/2} \approx 1.$$

The particular topography that we have chosen is shown schematically in Fig. 3. Mathematically, it is expressed as

$$z_s = \begin{cases} 0, & X \leqslant XLE, \\ \tan\gamma \left[\dfrac{\dfrac{-2DL}{\pi} \sin\left(\dfrac{\pi(X - XLE)}{2DL}\right) + (X - XLE)}{2} \right], & XLE \leqslant X \leqslant XL + DL, \\ \tan\gamma(X - XL), & XL + DL \leqslant X \leqslant XML, \\ \tan\gamma \left[\dfrac{\dfrac{XM - XML}{\pi} \sin\left(\dfrac{\pi(X - XML)}{(XM - XML)}\right) + (X - XML)}{2} + (XML - XL) \right], & XML \leqslant X \leqslant XM, \\ \tan\delta \left[\dfrac{\dfrac{XM - XMR}{\pi} \sin\left(\dfrac{\pi(X - XMR)}{(XM - XMR)}\right) + (X - XMR)}{2} - (XMR - XR) \right], & XM \leqslant X \leqslant XMR, \\ -\tan\delta(X - XR), & XMR \leqslant X \leqslant XR - DR, \\ -\tan\delta \left[\dfrac{-\dfrac{2DR}{\pi} \sin\left(\dfrac{\pi(X - XRE)}{2DR}\right) + (X - XRE)}{2} \right], & XR - DR \leqslant X \leqslant XRE, \\ 0, & X \geqslant XRE, \end{cases} \tag{2-27}$$

where

$$|XLE - XL| = DL, \quad |XRE - XR| = DR,$$
$$|XMR - XM| / |XM - XML| = \tan\gamma/\tan\delta.$$

It can be seen that this approximates a linear ridges of slopes, γ, δ, respectively. z_s is also seen to be continuous, with continuous first and second derivative. The actual parameters that we have chosen are:

$$D = H = 7 \text{ km}, \quad XL = 1.7 \text{ km}, \quad XM = 3.5 \text{ km}, \quad XR = 5.3 \text{ km}.$$
$$DL = 1 \text{ km}, DR = 1 \text{ km}, |XM - XML| = |XM - XMR| = 1 \text{ km}, \gamma = \delta = 45°.$$

The height of the summit $z_{s\max.}$ is, according to (2-27), ≈ 1.3 km. This topography seems suitable for proving the viability of our method, since the slope varies continuously from 0° to 45° and then decreases continuously until it reaches 0° at the summit. When the quantities z_s, $\partial z_s/\partial x$, $\partial^2 z_s/\partial x^2$, are scaled and nondimensionalized with respect to $z_{s\max.}$, they are seen to be of the same order of magnitude, i.e., $\approx 1, 1, \pi z_{s\max.}/2DL$. Therefore the second derivative is not large compared to the first derivative. This latter property is essential, since linear stability properties strongly depend on the fact that the extra nonderivative terms are $O(\Delta t)$, and the transformation is nonsingular.

If the initial condition on the potential temperature indicates a stable environment, an additional precautionary step is necessary. It must be realized that in that case the pressure still contains hydrostatic terms given by:

$$\partial p_H/\partial z = (\rho g/\theta_0)\,\theta)_{t=0}\,.$$

Consequently, one can subtract these hydrostatic terms from the pressure gradient and the buoyancy force $B(\theta)$, respectively (see Eqs. (2-1-b) and (2-1-c)). By doing so, the truncation errors associated with transformed coordinates can be minimized [10].

When the above-mentioned constraints have been taken into account, requirements (a)–(c) are satisfied. While it is a straightforward matter to check the fulfillment of (b) and (c), there is no general way to estimate truncation errors, especially those due to aliased interaction [6]. In the case of thermal convection, Fox [6] has found that the appearance of physically impossible negative deviations of potential temperature is an indication of large truncation errors. In general, if viscosity and diffusion are large enough, this kind of truncation error can be avoided. Our numerical experiments have shown that the minimum nonlinear eddy viscosity [3, 7] needed to prevent negative deviations of potential temperature is the same for zero and nonzero topography. In the absence of explicit viscosity the parameters α, β (Eq. (2-24)) can be used to add an implicit smoothing and thereby eliminate negative temperature deviations. It has been found that the minimum values of α and β which are necessary to achieve the above requirements are the same with and without topography.

It is well known [19] that in the case of no topography and constant basic density, the staggered-mesh configuration and centered time and space differencing will, in the absence of normal fluxes, assure quasiconservation of quadratic quantities, thereby eliminating implicit smoothing. In the transformed domain the convective terms contain extra nonderivative terms. Therefore quasiconservation has to be checked empirically. In order to compare between numerical and real diffusion, we performed the following consistency check. With the topography defined in (2-27), we set $K_H = K_M = 0$ and $\alpha = \beta = \frac{1}{2}$ (see Eqs. (2-6-a-b), (2-23) and (2-24)). We then

specified an initial perturbation $\theta = f(\bar{x}, \bar{z})$, with θ max $\leqslant 1$ deg. The time step was governed by (2-25) with $b = 1$, but Δt was not allowed to exceed 10 sec. An upper bound of 10 sec for this case of an initially specified "hot-spot" was necessary, since this is a physically unstable situation with a fast rate of development. We then performed calculations with various initial conditions, and in all of them quadratic quantities were conserved to within 1 % throughout the approximately 15 min of simulated time. The quantity $\rho_0 G^{1/2}\theta^2$ was better conserved than total energy, probably because the difference scheme quasiconserves temperature variance.

With the values $\alpha = \beta = \frac{1}{2}$, the calculations eventually became unstable, even with flat topography ($z_s = 0$), and $\rho = \text{const}$, in which case *all* quadratic quantities are quasiconserved. This is apparently typical with difference schemes which quasiconserve quadratic quantities [11]. When the values $\alpha = 0.6$ and $\beta = 0.51$ are used, no blow-up occurs. For these values of α and β, implicit (built-in) smoothing is present. Nevertheless, when comparing this smoothing with the nonlinear eddy viscosity prescription recommended by Deardorff [3], we have found that this latter smoothing is about an order of magnitude greater than the implicit smoothing.

Having made consistency checks, we next perform some numerical experiments of meteorological significance to demonstrate the viability of our method.

III. Application to Meteorology

3.1. *Summary of Observations*

The numerical method outlined in the previous sections has been applied to simulate the meteorological phenomena of mountain up-slope winds. A detailed meteorological discussion of the phenomena has been given by Orville [21] and Gal-Chen [7]. The observed general features of the phenomena are:

(a) Despite the fact that the potential temperature deviations from reference atmospheres (hydrostatic but not necessarily adiabatic) are decreasing up-slope, the flow near the ground is up-slope (countergradient).

(b) Secondary weak circulation is sometimes observed at points neighboring a mountain.

(c) The depth of the up-slope winds increases with distance up the slope.

(d) In a stable atmosphere the lower layer may eventually become unstable (due to heating). The depth of the unstable layer increases up-slope. Above the unstable layer is an almost adiabatic layer, and above this is the stable layer.

These features have successfully been simulated in our numerical experiments.

3.2. *Specifications of the Experiments*

The calculations are performed on a vertical plane 7 × 7 km with the topography specified by (2-27). This topography seems suitable for demonstrating the generality and viability of the method, since it has a variable slope. The reference potential temperature is $\theta_0 = 296°\text{K}$. A grid of 71 × 71 points is constructed in the $\bar{x}$, $\bar{z}$ plane. The grid spacing as viewed by a Cartesian observer is of course variable, but on the order of 100 m. The distribution of variables on the grid has been described in detail in Section II. The boundary conditions for the momentum equations are "free slip" along all boundaries. Thus, no drag is modeled at the lower boundary.

The boundary conditions for the potential temperature are no heat fluxes at lateral boundaries and constant potential temperature at the top.

To calculate the potential temperature deviation at the lowest grid point, the following parametric procedure has been used. It is first postulated that the distance between the lowest grid points $(i, 1)$, and the ground $(i, \frac{1}{2})$ is $\Delta\bar{z}/2$. Next, the potential temperature deviations at the ground $(i, \frac{1}{2})$, are specified as:

$$\theta)_{\bar{z}=0} = \bar{\theta}(z)_{\bar{z}=0} + (7 - 4(z_s/z_{s\max}))\, S(\bar{x}) \sin(\pi(T/12)). \tag{3-1}$$

$\bar{\theta}(z)$ represents the initial potential temperature stratification (to be specified later), T is time in hours, $z_{s\max}$ is the height of the summit, z_s is the topography and $z = z(\bar{x}, \bar{z})$ is the z coordinate. $S(\bar{x})$ is a function which specifies whether the mountain is being heated symmetrically or asymmetrically. If the heating is symmetric,

$$S(\bar{x}) = 1. \tag{3-2}$$

If it is asymmetric,

$$S(\bar{x}) = \begin{cases} 1, & \bar{x} \leqslant 3.5 \text{ km}, \\ 1/2 \cos[(\bar{x} - 3.5)\, 2\pi/3.5] + 1/2, & \bar{x} \geqslant 3.5 \text{ km} \end{cases}. \tag{3-3}$$

Then at a given time level, by knowing the potential temperature perturbation at the ground $\theta_{i,1/2}$, and the potential temperature perturbation at the lowest grid point $\theta_{i,1}$, we can calculate the heat flux in the following way. First we calculate the quantity

$$\bar{H}^3_{i,3/4} = G^{33}[(\theta_{i,1} - \theta_{i,1/2})/(\Delta\bar{z}/2)] + (G^{13})_{i,1}(\theta_{i+1,1} + \theta_{i+1,1/2} - \theta_{i-1,1} - \theta_{i-1,1/2})/4\Delta\bar{x}$$

(Eq. (2-3-b)). Then, from the value of $(K_H)_{i,1/2}$ and assuming that the heat flux in the boundary layer is independent of the height above the ground, the heat flux at the lowest grid point can be calculated and therefore the temperature at the lowest grid point can be calculated. At the lowest grid point, therefore, both advective cooling or warming and turbulent diffusion are present.

This treatment of the lower boundary is much like that used by Orville [20]. The deficiencies of this treatment have been mentioned in paper I, Section 2.4. Nevertheless, the more realistic approach of identifying the lower grid point with the ground, and imposing "no-slip" there, has been tried unsuccessfully by Orville [20]. His failure was possibly due to insufficient resolution. At any rate, the prescription just outlined is mathematically well posed and can be viewed as a parameterization of heat flux.

The model atmosphere is initially at rest, and the potential temperature deviation at the ground drives the motion. Two types of initial stratification $\bar{\theta}(z)$ have been used. The first is a neutral atmosphere, in which $\bar{\theta})_{t=0} = 0$. The second is a moderately stably stratified atmosphere, with stability ST, given by:

$$\mathrm{ST} = (\partial\bar{\theta}/\partial z))_{t=0} = 1 \text{ deg/km}.$$

Thus, in cgs units and in the $\bar{x}, \bar{z}$ coordinates,

$$\bar{\theta})_{\bar{z}=0} = \theta_0 + 10^{-5}((\bar{z}(H - z_s)/H) + z_s).$$

It is important to note that in the actual computation, the constant θ_0 is always subtracted out and the perturbation is calculated. This is done to avoid large truncation error. In Section 2.5 we have listed other precautionary measures to avoid large truncation errors.

In the diffusive terms of the temperature equation, but not in the advective terms, we treat the temperature as a deviation from the reference hydrostatic temperature $\bar{\theta}(z)$. Otherwise, the calculated turbulent heat fluxes in a stable atmosphere will be downward, contrary to observation and theory, which suggest that the heat flux in a stable atmosphere is countergradient [4].

The time step is determined by (2-25) and (2-26) with $b = 0.9/(2 \max(\alpha, \beta))$; α and β control the amount of implicit smoothing. The values $\alpha = 0.55$, $\beta = 0.51$ are used. An upper limit of 50 sec has been imposed on the time step. The nonlinear eddy viscosity concept has been applied throughout the calculation (e.g., [3, 7]).

We have performed five experiments. The experiments with their parameters are listed in Table I. The computations were done on an IBM 360/95 and took approximately 15 hr of machine time. On the average it took about 1 hr of machine time to simulate 2 hr of real time.

A symmetric perturbation is a perturbation given by (3-1) with $S(\bar{x}) = 1$. An asymmetric perturbation is also given by (3-1), but with $S(\bar{x})$ given by (3-3).

A momentum stream-function for display purposes has been calculated. The stream function is shown in units of 10^2 gm cm^{-1} sec^{-1}. The time in minutes is shown in the upper-left corner of the figures, and the experiment number in the upper-right corner.

TABLE I

List of the Numerical Experiments and Their Parameters

Expt	Type of perturbation	Type of atmosphere	$\sigma^{-1} = K_H/K_M$
1	Symmetric	Neutral ($\partial\theta/\partial z = 0$)	1
2	Symmetric	Stable ($\partial\theta/\partial z = 1$ deg/km)	1
3	Symmetric	Stable ($\partial\theta/\partial z = 1$ deg/km)	3
4	Asymmetric	Neutral	1
5	Asymmetric	Neutral	3

3.3. *Results of the Experiments*

The results of Expt 1 are shown in Figs. 4–9. This case is characterized by relatively rapid development. After 30 min (Fig. 4), the vortex center (the stream function center), which originates near the bottom of the slope, is close to the summit and continues rising uphill. After 30 min, the potential temperature above the plain is still rather uniform (Fig. 5). After 45 min (Fig. 6), the vortex center is about 2.5 km high, i.e., ~1.2 km above the summit, and it is moving away from the axis of symmetry. By that time a secondary circulation has been developed in the plain, but it is too weak to be seen on the stream function plot. At this stage, the secondary circulation is apparently not affected by the lateral boundaries, which are still motionless. As a further check of this conjecture we have moved the lateral boundaries further away by adding more mesh points and we still get secondary circulation after 45 min. Inspection of the temperature field after 45 min (Fig. 7), shows that at the plain grid points nearest the slopes, advective cooling is at work. The horizontal uniformity over the plain is therefore gradually being destroyed. This happens despite the fact that the plain is heated uniformly. Above the summit, the isentropes attain a mushroom shape. After 60 min. (Fig. 8), the stream function center continues to move away from the axis of symmetry. The secondary circulation is well developed by that time. The isentrope contours (Fig. 9) show that the cap continues to rise and is quite close to the top. Another cap is in the process of development at the side boundaries. We have already seen that after 45 min advective cooling at plain points which neighbor the slope has caused horizontal nonuniformity. Fifteen min later, as a result of this horizontal nonuniformity, a warm bubble can be seen 0.5 km above the ground (Fig. 9). This warm bubble is the 0.45 contour, just above the plain. The developemnt and history of the main circulation is similar to that of Orville [20]. Nevertheless our overall picture is less diffused, and less smoothed. The main difference between our case and Orville's case is that no sign of a secondary circulation can be seen in his

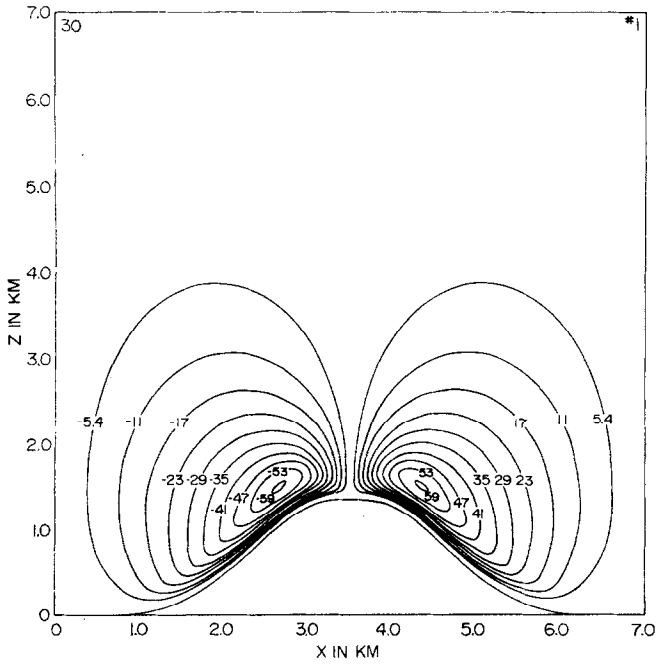

FIG. 4. Stream function field after 30 min for Expt 1.

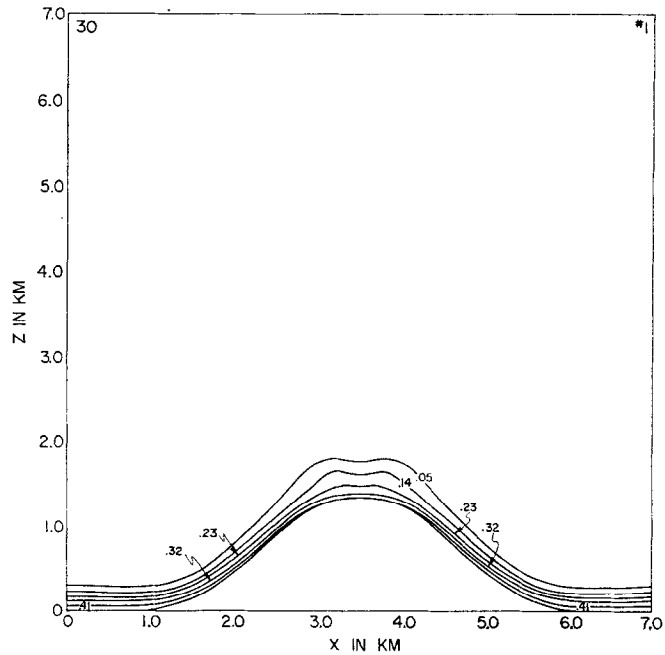

FIG. 5. Potential temperature deviations after 30 min for Expt 1.

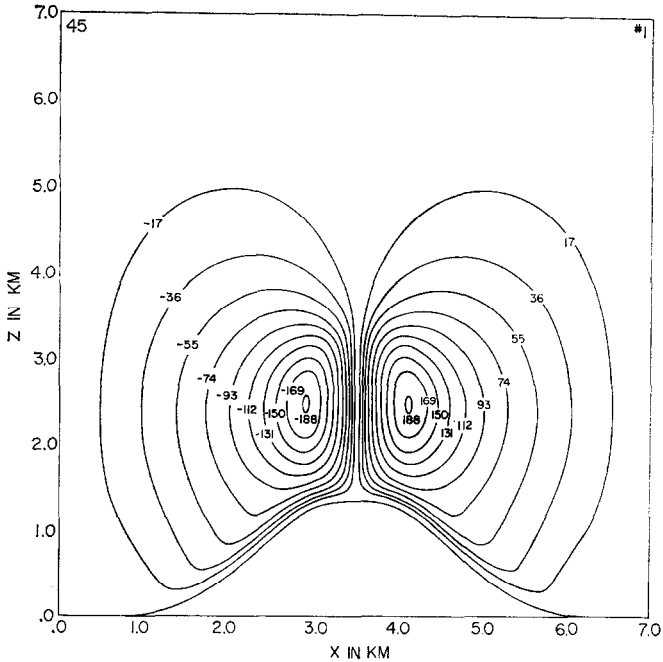

FIG. 6. Stream function field after 45 min for Expt 1.

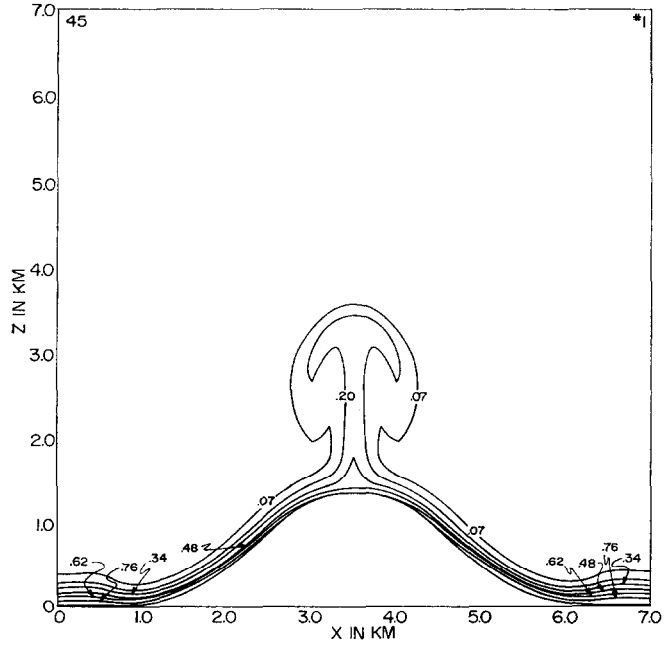

FIG. 7. Potential temperature deviations after 45 min for Expt 1.

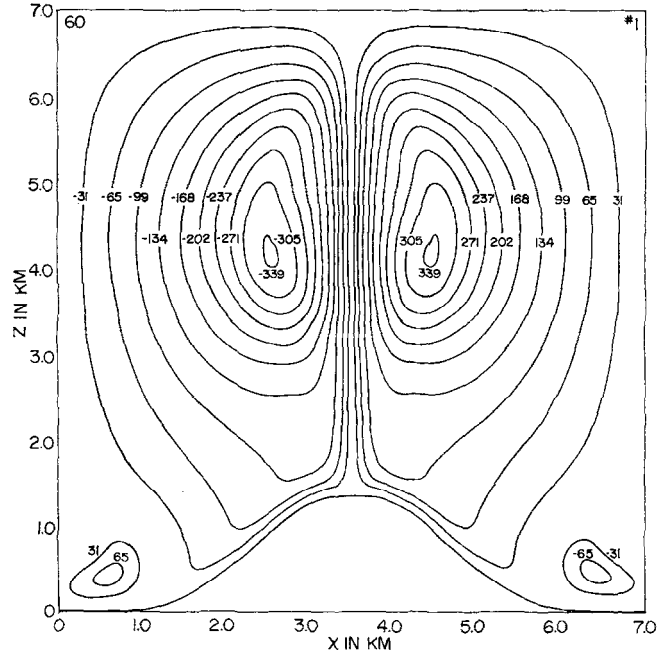

FIG. 8. Stream function field after 60 min for Expt 1.

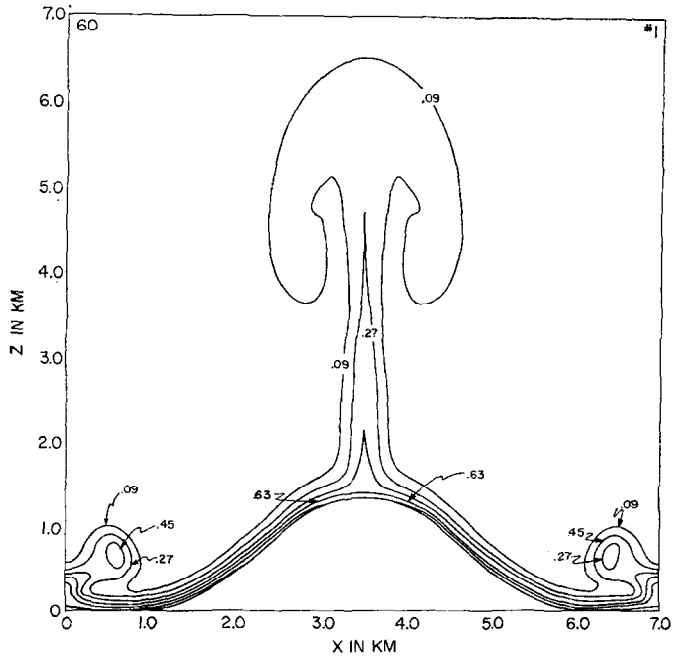

FIG. 9. Potential temperature deviations after 60 min for Expt 1.

results. This is probably due to the fact that his implicit diffusion is large enough to compensate for advective cooling, and the shape of isentropes above the plain in his case continues to be dominated by the uniform heating of the ground. Experiment 1 was integrated up to 90 min. The results after more than 60 min are not shown graphically, since at this stage the top boundary had considerably affected the motion. The flow fields, however, are computationally stable.

The results of Expt 2 are dramatically different from those of Expt 1. Due to the environmental stability, it has a slower rate of development.

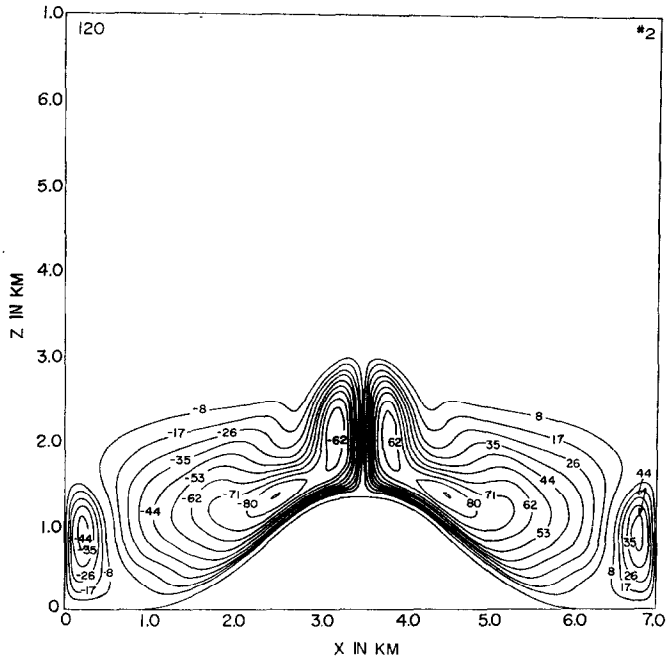

FIG. 10. Stream function field after 120 min for Expt 2.

The results of Expt 2 after 120 min are shown in Figs. 10–11. By that time the secondary circulation is well developed (Fig. 10). The first signs of a secondary circulation, however, appear after 90 min. The circulations are still confined to the lower atmosphere. As time advances, the isentropes above the summit (Fig. 11) become tighter. The stability is therefore increased, and it is more difficult for the convection to penetrate. Another characteristic of Expt 2 (Fig. 11) is that the stability of the lower parts of the atmosphere is destroyed. The depth of the unstable layer is increasing upslope (in agreement with Fosberg's observation [21]).

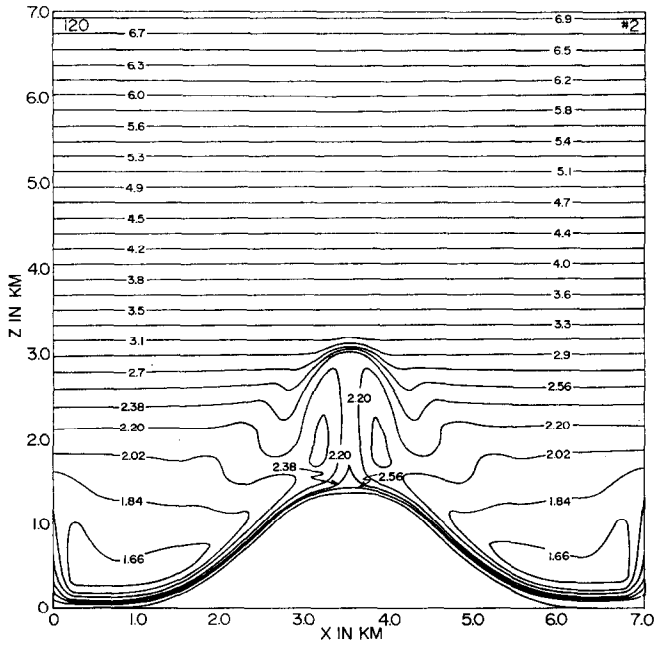

FIG. 11. Potential temperature deviations after 120 min for Expt 2.

The results of Expt 3 (in which $K_H/K_M = 3$ instead of 1) are a further indication of the crucial part that eddy diffusion plays in enhancing the motion and in controlling the secondary circulation.

Some results of Expt 3 are displayed in Figs. 12–15. After 120 min, the main circulations are more developed than in Expt 2 at that time. The main circulation has been extended to the side boundaries (Fig. 12), and the *secondary circulation never appears*. By this time, the chances that a secondary circulation will eventually appear are very small, since the return flow at the plain, together with diffusion, is now strong enough to counterbalance advective cooling. Except for the disappearance of the secondary circulation, the isentrope pattern of Expt 3 (Fig. 13), in the main cell, is very much like that of Expt 2. Above the summit, the result of the penetrating convection is an increased stability of the atmosphere (Fig. 15), just above the convective layer, which will further inhibit convection. Figure 15 reveals that in general, three layers are seen now to exist: a superadiabatic lower layer; an almost adiabatic layer just above; and a stable layer on top. This feature is in agreement with observation (e.g., Orville [21]). Above the summit and the upper slopes, the stable layer is actually an inversion lid. Further down-slope the stability is moderate to weak.

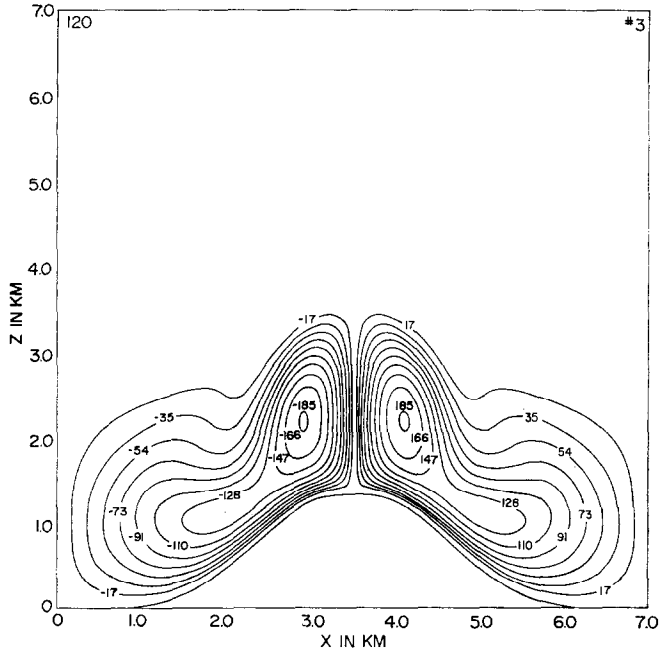

FIG. 12. Stream function field after 120 min for Expt 3.

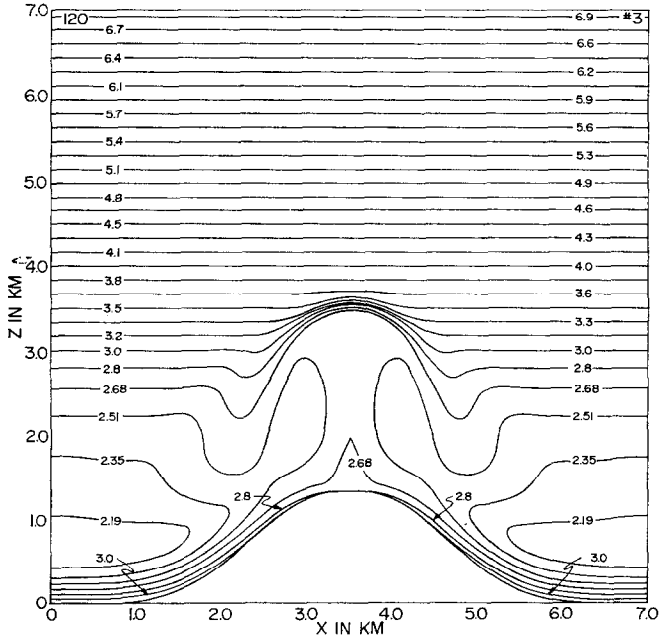

FIG. 13. Potential temperature deviations after 120 min for Expt 3.

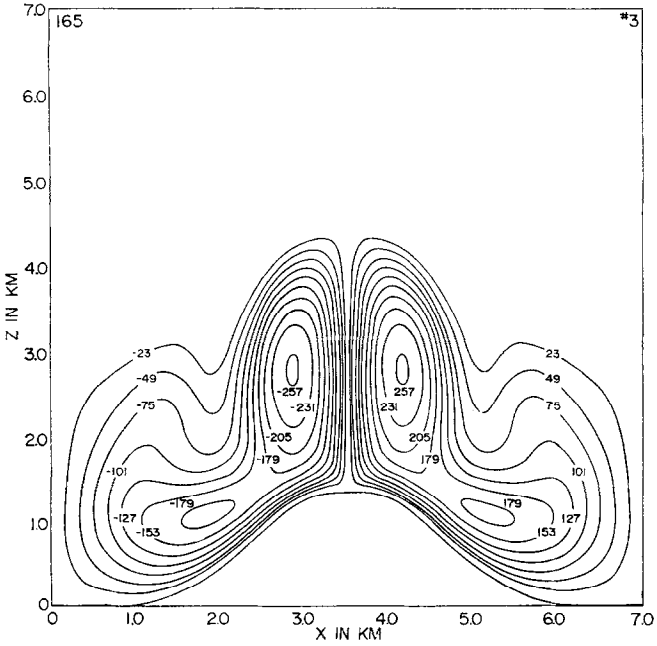

FIG. 14. Stream function field after 165 min for Expt 3.

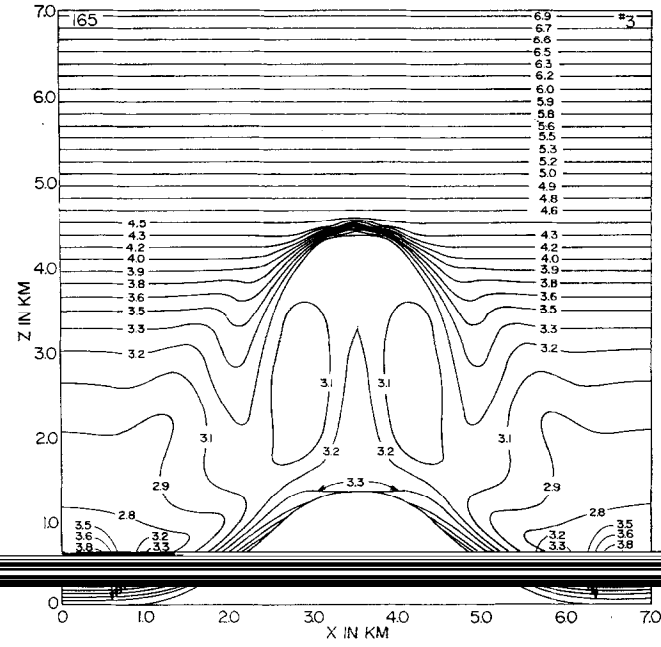

FIG. 15. Potential temperature deviations after 165 min for Expt 3.

The inversion lid which is eventually created is very similar to an inversion which sometimes occurs above hot cities during summer (the "heat island" effect). In both cases, the reason for the inversion is strong differential heating, combined with atmospheric stability and modified by orographic effects. Such an inversion over a city tends to trap pollutants.

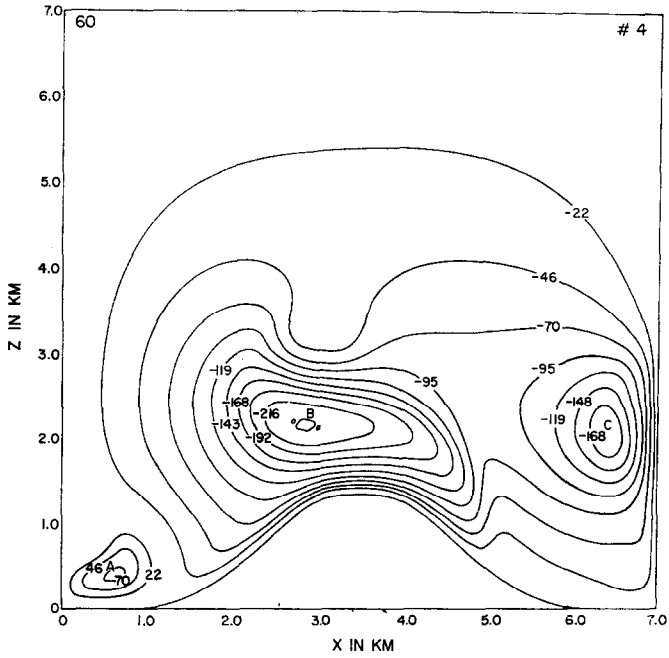

FIG. 16. Stream function field after 60 min for Expt 4.

Experiment 4 is different from Expt 1 in that asymmetric heating has been imposed. The results are shown in Figs. 16–19. Early in the integration, two main cells of uneven magnitude existed side by side. Very soon, however, larger horizontal velocities developed in what was formerly the axis of symmetry. After 60 min (Fig. 16), the smaller cell has been entirely consumed by the larger one, and at the right-hand side of the boundary, a new cell has developed due to uneven heating on the right plain. This cell is more evident in the isentropes in Fig. 17, which show a conspicuous mushroom at the right boundary. This mushroom is very similar to the bubble cell in Lilly's [18] numerical experiment, and it is not very much influenced by the slope. Above the summit, the perturbation rises only a little, and is swept to the right. The secondary circulation, which has developed in the lower left-hand corner, is similar to the one in the analogous symmetric case (Expt 1,

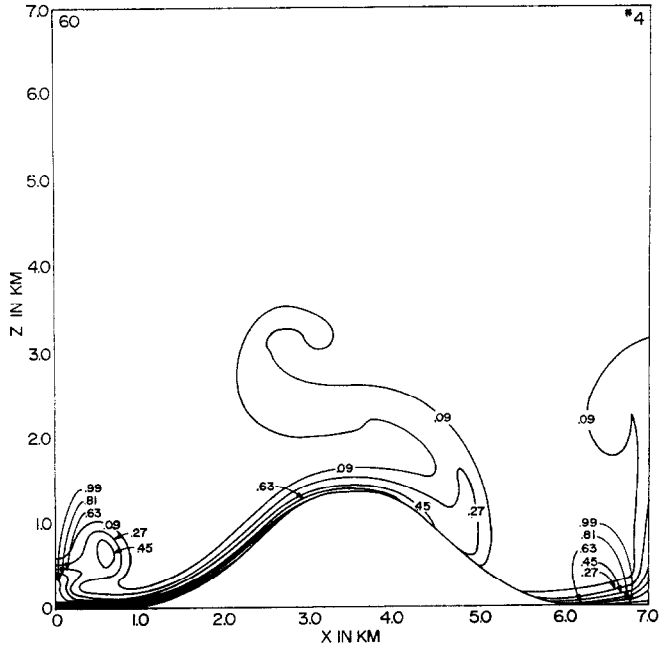

FIG. 17. Potential temperature deviations after 60 min for Expt 4.

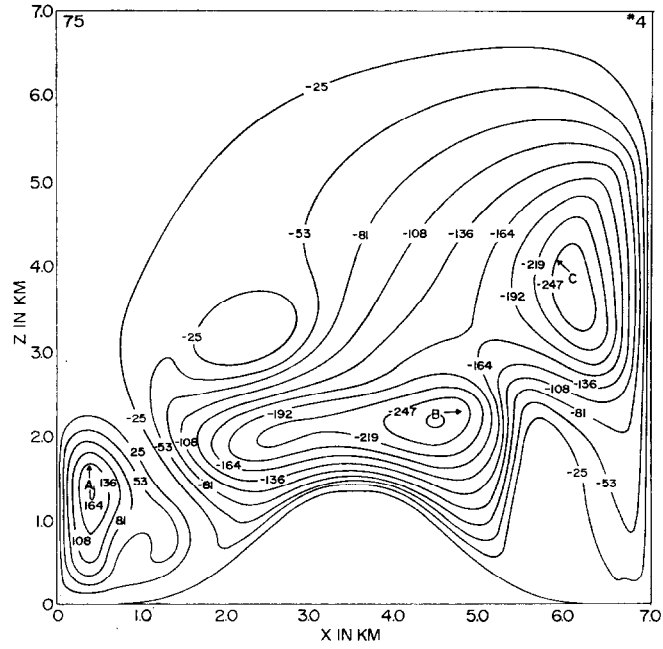

FIG. 18. Stream function field after 75 min for Expt 4.

Fig. 8). (Note that in Eq. (3-3), $S(\bar{x}) = 1$ for $x \leqslant 3.5$.) This is a further indication that the secondary circulation develops because of advective cooling, which upsets the uniform heating, and not because of mechanical convergence.

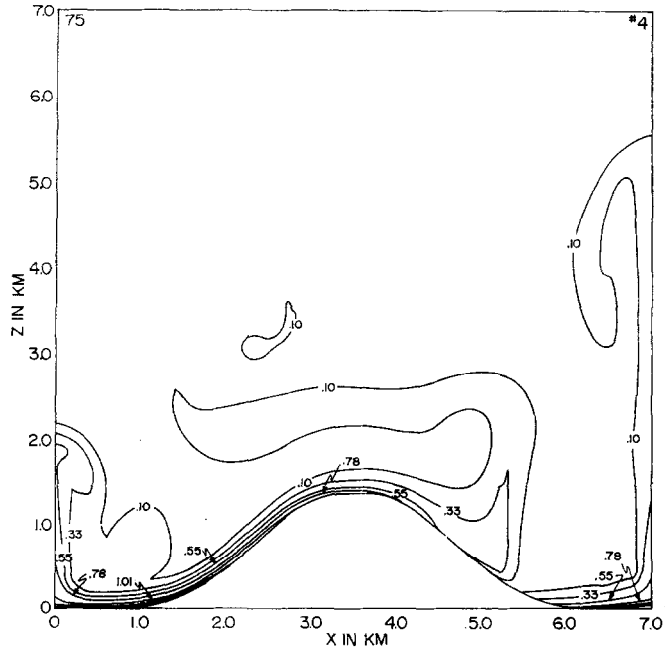

FIG. 19. Potential temperature deviations after 75 min for Expt 4.

Figures 18–19 show the results of Expt 4 after 75 min. The general features are that cell *C* further rises and moves to the left, cell *B* further moves to the right, and the secondary circulation *A* is further developed.

Experiment 5 (Figs. 20-22) differs from Expt 4 by having greater eddy thermal diffusion, although an unaltered prescription for eddy viscosity. The growth is therefore faster than in Expt 4. Cells *A*, *B* and *C* in Fig. 21 are seen to be more developed than their analogs in Expt 4. Cell *C* is higher.

A feature common to all these experiments is that the depth of the up-slope winds increases with distance up the slope. This feature is in agreement with Defant's observation [21]. The magnitude of the up-slope winds near the summit at the end of Expt 3 (after 165 min) is 7–8 m sec^{-1}. This is in agreement with Defant's observations which were done in a stable environment.

The results of Expts 2 and 3 indicate that a stable atmosphere can be integrated for an extended time, with virtually no artificial numerical effects of interaction

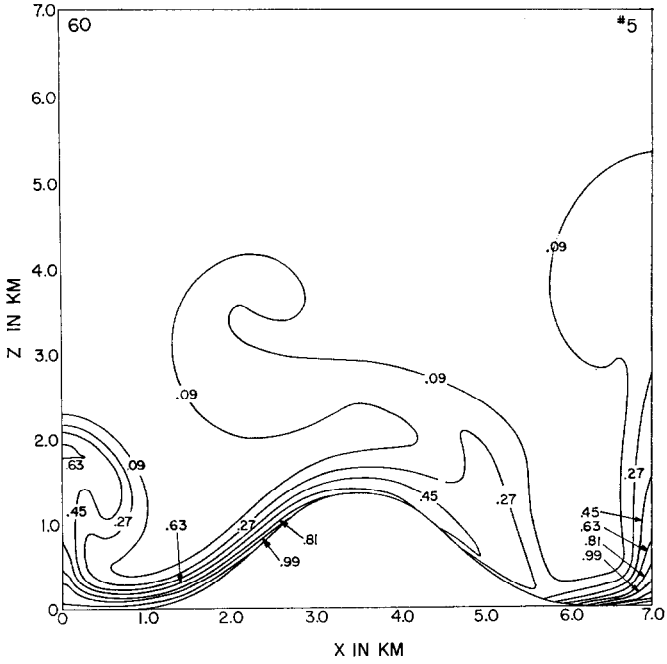

FIG. 20. Potential temperature deviations after 60 min for Expt 5.

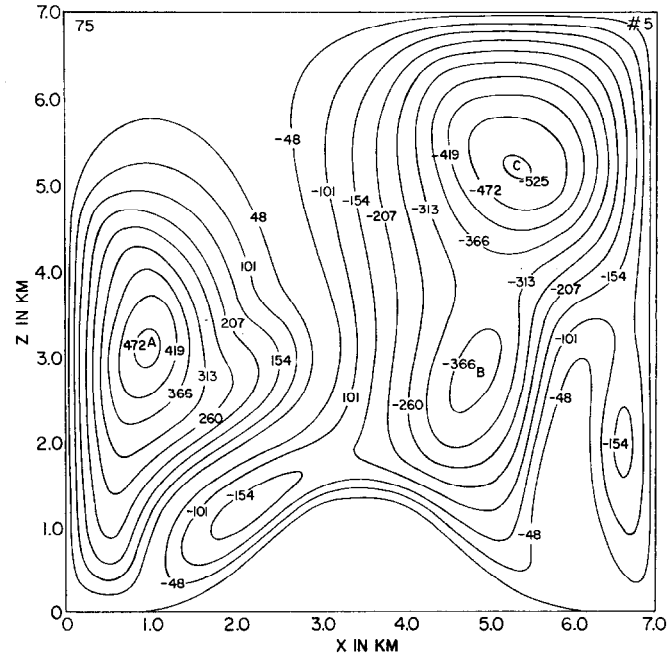

FIG. 21. Stream function field after 75 min for Expt 5.

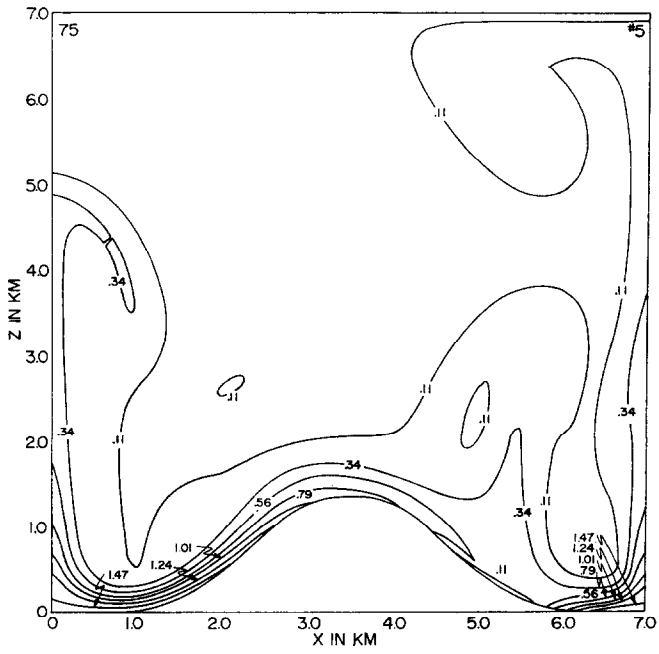

FIG. 22. Potential temperature deviations after 75 min for Expt 5.

with the top boundary. Numerical interaction of the secondary circulation with the lateral boundary occurs both in the stable and neutral case. However, the lateral boundaries do not initiate the secondary circulation, nor do they modify its early development.

IV. CONCLUSIONS

Numerical simulation of convection is considered a difficult problem, even without topography. Yet in this work we were able to include topography in a quite general way.

The major computational difficulty in calculating nonhydrostatic flow above terrain is associated with the fact that in Cartesian coordinates the lower boundary is irregular. As a result, it is very difficult to incorporate the correct boundary conditions, and it is necessary to define special mesh points near the boundary. Consequently, such calculations often have a somewhat narrow range of applicability (e.g., simple geometry or steady-state assumption). Our coordinate transformation enables us to devise a numerical method which overcomes these difficul-

ties. The major conclusion is, therefore, that the range of applicability of "conventional" difference schemes has been extended to arbitrary topography, with continuous second derivatives.

The results of our computations demonstrate the viability of our method. The general small-scale characteristics of mountain up-slope winds have been simulated. In addition, the results have demonstrated the crucial role played by the exchange coefficients and the environmental stability, in determining both the quantitative and qualitative features of the circulations.

Our method should be applicable to other hydrodynamical problems in which the lower boundary is irregular.

ACKNOWLEDGMENTS

This work, based largely on Tzvi Gal-Chen's Ph.D. thesis, was supported by NASA Grant NGR 33-008-191 to Columbia University. The computations were carried out on the IBM 360/95 computer at the Goddard Institute for Space Studies (GISS), New York, NY. We thank Drs. R. Jastrow, K. Grossman, and M. Halem for their support.

This manuscript was professionally and skillfully typed by Ms. J. Prangley and Ms. U. Rosner.

REFERENCES

1. A. J. CHORIN, *Math. Comp.* **22** (1968), 745.
2. J. W. DEARDORFF, *J. Fluid Mech.* **41** (1970), 453.
3. J. W. DEARDORFF, *J. Computational Phys.* **7** (1971), 120.
4. J. W. DEARDORFF, *J. Geophys. Res.* **77** (1972), 5900.
5. L. FOX, "Numerical Solution of Ordinary and Partial Differential Equations," Pergamon, Oxford/London/Paris. Addison–Wesley, 1962.
6. D. FOX, *J. Atmos. Sci.* **29** (1972), 322.
7. T. GAL-CHEN, Numerical Simulation of Convection with Topography, Ph.D. Thesis, Columbia University, New York, 1973.
8. T. GAL-CHEN AND R. C. J. SOMERVILLE, *J. Computational Phys.* **17** (1975), 209–228.
9. J. GARY, *Math. Comp.* **18** (1964), 1.
10. J. GARY, *J. Atmos. Sci.* **30** (1973), 223.
11. A. GRAMMELTVELDT, *Mon. Weather Rev.* **97** (1969), 384.
12. B. GUSTAFSSON, *J. Computational Phys.* **7** (1971), 239.
13. F. H. HARLOW AND A. A. AMSDEN, *J. Computational Phys.* **8** (1971), 197.
14. F. H. HARLOW AND J. E. WELCH, *Phys. Fluids* **8** (1965), 2182.
15. H. B. KELLER, *SIAM J. Numer. Anal.* **2** (1965), 281.
16. [illegible]
19. D. K. LILLY, *Mon. Weather Rev.* **93** (1965), 11.
20. H. D. ORVILLE, *J. Atmos. Sci.* **21** (1964), 622.

21. H. D. ORVILLE, Orographic convection, *in* "Thermal Convection: A Colloquium," NCAR-TN-24, pp. 385–430, National Center for Atmospheric Research, Boulder, CO, 1967.
22. R. D. RICHTMYER AND K. W. MORTON, "Difference Methods for Initial-Value Problems," 2nd ed., Interscience, New York, 1967.
23. S. SCHECHTER, *Quart. Applied Math.* **18** (1960), 285.
24. R. C. J. SOMERVILLE, Numerical Simulation of Small-Scale Thermal Convection in the Atmosphere, *in* "Proc. Third Intern. Conf. Numerical Methods in Fluid Dynamics," 1973, Vol. II, Springer–Verlag ("Lecture Notes in Physics," Vol. 19, pp. 238–245).
25. J. T. STEINER, *J. Atmos. Sci.* **30** (1973), 414.
26. R. VARGA, "Matrix Iterative Analysis," Prentice–Hall, Englewood Cliffs, NJ, 1962.
27. G. P. WILLIAMS, *J. Fluid Mech.* **37** (1969), 727.